Determination of Aggregate Elastic Properties of Powder-Beds in Additive Manufacturing Using Convolutional Neural Networks

Ardalan R. Sofi
Department of Mechanical and Aerospace Engineering, University of California at Davis, CA, USA

Bahram Ravani[1]
Department of Mechanical and Aerospace Engineering, University of California at Davis, CA, USA

Abstract

The most popular strategy for the estimation of effective elastic properties of powder-beds in Additively Manufactured structures (AM structures) is through either the Finite Element Method (FEM) or the Discrete Element Method (DEM). Both of these techniques, however, are computationally expensive for practical applications. This paper presents a novel Convolutional Neural Network (CNN) regression approach to estimate the effective elastic properties of powder-beds in AM structures. In this approach, the time-consuming DEM is used for CNN training purposes and not at run time. The DEM is used to model the interactions of powder particles and to evaluate the macro-level continuum-mechanical state variables (volume average of stress and strain). For the Neural Network training purposes, the DEM code creates a dataset, including hundreds of AM structures with their corresponding mechanical properties. The approach utilizes methods from deep learning to train a CNN capable of reducing the computational time needed to predict the effective elastic properties of the aggregate. The saving in computational time could reach 99.9995% compared to DEM, and on average, the difference in predicted effective elastic properties between the DEM code and trained CNN is less than 4%. The resulting sub-second level computational time can be considered as a step towards the development of a near real-time process control system capable of predicting the effective elastic properties of the aggregate at any given stage of the manufacturing process.

2012 ACM Subject Classification Applied computing → Industry and manufacturing

Keywords and phrases Additive Manufacturing, Convolutional Neural Network, Homogenization, Discrete Element Method, Powder-Bed

Digital Object Identifier 10.4230/OASIcs.iPMVM.2020.8

Funding This work was partially supported by a Space Technology Research Institutes grant from NASA's Space Technology Research Grants Program.

1 Introduction

Over the past few decades, additive manufacturing (AM) has become one of the mainstream manufacturing processes. Unlike the conventional subtractive manufacturing methods, AM is based on a layer-wise transformation of materials into the three-dimensional workpiece; therefore, it does not require fixtures, cutting tools, or other specialized tooling equipment. One of the most rapidly growing AM technologies to manufacture complex metallic and ceramic structures is Selective Laser Sintering (SLS), where a high-power laser fuses small powders into a desired three-dimensional (3D) shape. Physical modeling of powder-based AM structures is challenging due to the discrete nature of their structures. Several researchers modeled the powder bed as a continuum structure using FEM. However, as the number of required elements for particle-level modeling of large discrete structures increases, the

[1] Corresponding author

2nd International Conference of the DFG International Research Training Group 2057 – Physical Modeling for Virtual Manufacturing (iPMVM 2020).
Editors: Christoph Garth, Jan C. Aurich, Barbara Linke, Ralf Müller, Bahram Ravani, Gunther Weber, and Benjamin Kirsch; Article No. 8; pp. 8:1–8:17

OpenAccess Series in Informatics
Schloss Dagstuhl – Leibniz-Zentrum für Informatik, Dagstuhl Publishing, Germany

FEM becomes more computationally expensive. We modeled the bounded pair of powders in an AM structure as truncated spherical particles with elastic bonding. Every elastic-bound constitutes a 3D beam element between the centers of two powders; therefore, the manufactured aggregate constructs a space frame structure. An explicit expression of the symmetric stiffness matrix of the beam element is derived, and the force-displacement behavior of AM structure is modeled using the DEM. The macro-level volume average of the stress and strain tensor is found based on micro-level variables such as grain displacements and local geometrical characteristics. Therefore, the developed DEM code could be utilized to estimate the effective elastic properties of any powder-based AM parts. An alternative approach to such a homogenization method is to extract the appropriate set of patterns from the pixelated structure by convolving a weighted filter across the whole structure. Using the Convolutional Neural Network (CNN) technique, these features are then combined by the subsequent layers of CNN to detect higher-order features. The last fully-connected layer at the end of the network might be used to predict the elastic material properties of aggregate.

The effective implementation of powder-based AM technologies relies on the characterization of the final product based on manufacturing process parameters. These parameters include layer thickness, scanning strategy, and powder size and distribution [5]. Miranda et al. [23] studied the influence of laser scanning speed on the shear strength of stainless steel powder and developed a predictive regression model based on the manufacturing process parameters. Song et al. [35] investigated the effect of Selective Laser Melting (SLM) manufacturing process parameters on the microstructure of Ti6Al4V parts. Read et al. [30] used a statistical model to develop the experimental design for investigation of the effect of process parameters on the porosity formation in powder-based AM parts. Calignano et al. [4] used statistical techniques to study the relationship between surface roughness of parts produced by Direct Metal Laser Sintering (DMLS) and AM process parameters. Calignano et al. showed that scanning speed has a significant influence on the surface roughness of the final product. All mentioned experimental studies are expensive, time-consuming, and could be used to predict only specific properties of the final product based on the change of some particular process parameters.

FEM is the most largely used method for simulation of the thermomechanical behavior of powder beds at the scale of the part geometry. Using the SIMULIA simulation with a relatively large element size (0.2 mm), Yang et al. [40] studied the remained elastic strain in cantilever structures. Gu and He [10] developed an FEA model to evaluate the residual stresses of SLM manufactured parts. Gu and He concluded that the maximum residual stress in SLM parts was located at the end of the first and last track. Singh and Srinivasa [33] developed an FEA model to predict the density distribution in a single layer of powder and optimized process parameters for wanted density. Generally, the continuum model of powder bed using FEA is relatively faster than discrete models, although these continuum models are not capable of generating valid results for microstructural behavior of AM structures [8]. In order to analyze the microstructural behavior of AM structures, the mesh size for continuum models must be smaller than the size of particles. Hence, the microstructural molding of powder-based AM structures with FEA needs a large number of mesh elements; consequently, the FEA becomes even more computationally expensive than discrete models.

Developing a fast and accurate simulation tool for powder-based AM structures is challenging due to the stochastic nature of powdered material [9]. Therefore, a particle-based numerical model is required for the physical modeling of powder interaction during the additive manufacturing process [26]. One of the most accurate numerical techniques to study the mechanics of particle interactions is DEM [37]. Using DEM simulations, Haeri et al. [11] studied the influence of powder bed thickness and velocity of the powder spreading

devices on the surface roughness of the final AM structure. The DEM could even be used for elasticity analysis of continuum structures. For instance, Gao et al. [6] transferred the continuum structure into a discrete model and utilized the DEM model to analyze the force and displacement in the discretized structure.

Relating the macroscopic mechanical properties of AM parts to their microscopic structural properties is the essential goal of physical modeling of the powder-based additive manufacturing processes. The most popular strategy for the homogenization of material properties in AM structures is through FEM or DEM numerical solutions; however, these well-known homogenization techniques are time-consuming. Therefore, the homogenization of material properties in AM parts using FEM or DEM numerical techniques could limit our ability to develop a simulation-based real-time control system to improve the quality of the final product. Gobal and Ravani [8] reduced the computational time needed to simulate the thermo-mechanical behavior of the SLS manufactured structured by introducing the Adaptive Discrete Element Model (ADEM), where the size of discrete elements inside the powder bed increases in the areas far from the laser heat source. Liu and Shapiro [22] developed a mesoscale model of parts manufactured by a fused deposition process for homogenization of the elastic properties of AM structure [36]. Liu's homogenization technique computes the effective elasticity tensor of Fused Deposition Modeling (FDM) structures seven times faster than conventional finite element solvers. These homogenization methods are not fast enough to develop a simulation-based real-time control system for the AM process.

The Machine Learning (ML) methods, such as the fully-connected Artificial Neural Network (ANN) or Convolutional Neural Network (CNN), have been demonstrated to be valid ways to perform complex regression and pattern recognition for different manufacturing domains like process planning or production control [28]-[39]. Over the last decade, many studies have been done to use computer-vision hardware coupled with different neural network architecture to maximize performance in defect detection and defect classification in additive manufacturing process control. The interactions between the re-coater blade and powder bed during Laser Powder Bed Fusion (L-PBF) additive manufacturing process might cause re-coater hopping defect, super-elevation defect, etc. In order to autonomously detect spreading anomalies, Scime and Beuth [31] re-trained the already existing AlexNet CNN architecture using the transfer learning technique. Yuan et al. [41] set up a monitoring system and successfully applied semi-supervised CNN for in-situ monitoring of the SLM manufacturing process. In addition to the application of ML technique in computer-vision problems for AM, there has been limited work in the application of ML to predict the thermal behavior of AM structures (see [27]-[24]). To the best of our knowledge, in all the aforementioned works, there is no particle-level DEM simulation of powder-based AM structure combined with CNN algorithms to homogenize the effective elasticity tensor of powder-based AM structures.

2 Bounding Forces and Momentum of Partially Sintered Particle

The first step in the development of a DEM model to predict the effective elastic properties of powder-based AM structures for later training of the Neural Network is to evaluate the force-displacement behavior of every pair of sintered powder. Jefferson et al. [13] used FEA to derive the particle response rule for both normal and tangential relative deformation between every pair of particles and showed that this force-displacement model agrees with the Hertzian contact theory for small indentation. Then, Liu et al. [21] simplified Jefferson's formulation and modeled every pair of partially sintered powder as truncated elastic spheres overlapping neighboring particles with an elastic bridge that could transmit normal and tangential forces as well as rotational moments.

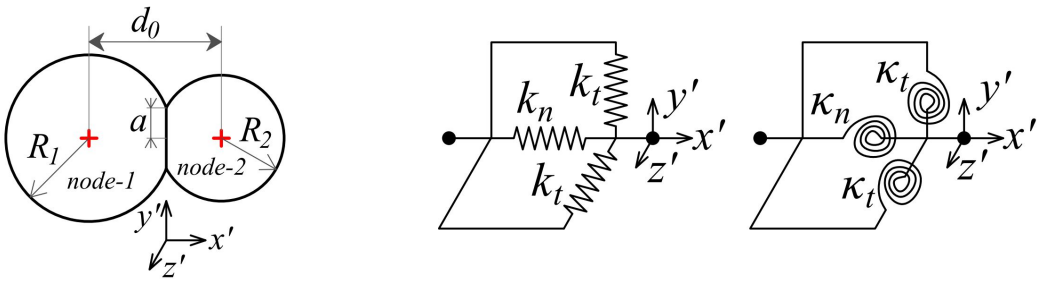

Figure 1 Schematic of a pair of sintered particles (left), and a system of two particles linked by six springs (right).

In this paper, the force-displacement between every pair of particles modeled using a single normal spring k_n, two identical tangential springs k_t, one torsional spring normal to the contact plane κ_n, and two identical torsional spring tangent to the contact plane κ_t (see Figure 1). Using the Liu et al. force-displacement model, Gobal [7] derived the following spring constants, which we used in our model:

$$k_n = \frac{Ea}{1-\nu^2}\left\{\frac{1+a^*\left[\frac{\pi}{6}\left(1-\nu^2\right)\left(1+2a^*\right)-a^*\right]}{\sqrt{\left(1-a^{*2}\right)}-\bar{\psi}\left(a^*+a^{*2}\left[\frac{\pi}{6}\left(1-\nu^2\right)\left(1+2a^*\right)-a^*\right]\right)}\right\} \tag{1}$$

$$k_t = \frac{2Ea}{(2-\nu)(1+\nu)}\left\{\frac{1+a^*\left[\frac{\pi}{6}\left(1-\nu^2\right)\left(1+2a^*\right)-a^*\right]}{\sqrt{\left(1-a^{*2}\right)}}\right\}, \tag{2}$$

$$\kappa_n = \frac{8ER^3a^{*3}}{(2-\nu)(1+\nu)}\left\{\frac{1+a^*\left[\frac{\pi}{6}\left(1-\nu^2\right)\left(1+2a^*\right)-a^*\right]}{\sqrt{\left(1-a^{*2}\right)}}\right\}, \tag{3}$$

$$\kappa_t = \frac{2ER^3a^{*3}}{(1-\nu^2)}\left\{\frac{1+a^*\left[\frac{\pi}{6}\left(1-\nu^2\right)\left(1+2a^*\right)-a^*\right]}{\sqrt{\left(1-a^{*2}\right)}-\bar{\psi}\left(a^*+a^{*2}\left[\frac{\pi}{6}\left(1-\nu^2\right)\left(1+2a^*\right)-a^*\right]\right)}\right\}, \tag{4}$$

where $a^* = a/R$ (a is the contact radius, $R^{-1} = R_1^{-1} + R_2^{-1}$, and $\bar{\psi}$ is a geometric factor that should be determined for each bond from the exact load distribution on the particle [13]. Liu et al. [21] tried several values of geometric factor and found $\bar{\psi} = 0.08$ to gave the best fit to the experimental data; therefore, We used the same value for our simulation. It is worth noting that a^* must be smaller than one ($a^* < 1$) to avoid the proposed stiffnesses in Eq. (1) to Eq. (4) turning into complex numbers.

3 Local and Global Stiffness Matrix for DEM Analysis of AM structure

Gao et al. [6] constructed a beam element within every two neighboring nodes with five degrees of freedom (DoF) per node and obtained a 10×10 symmetric stiffness matrix of the local equivalent beam element using the unit displacement method.Again Gobal [7] considered a 12 DoF force-displacement model ($\mathbf{f}' = \mathbf{K}'\mathbf{u}'$) which we are using here. This force-displacement model is between two particles where the displacement vector is

$\mathbf{u}' = (u'_1, u'_2, ..., u'_3)$ and force vector is $\mathbf{f}' = (f'_1, f'_2, ..., f'_3)$. Using the unit displacement method, Gobal [7] developed the local stiffness matrix as follows:

$$\mathbf{K}' = \begin{bmatrix} \mathbf{K'}_{11} & \mathbf{K'}_{12} \\ \mathbf{K'}_{21} & \mathbf{K'}_{22} \end{bmatrix}, \tag{5}$$

where

$$\mathbf{K'}_{11} = \begin{bmatrix} k_n & 0 & 0 & 0 & 0 & 0 \\ 0 & k_t & 0 & 0 & 0 & k_t d_0 \\ 0 & 0 & k_t & 0 & -k_t d_0 & 0 \\ 0 & 0 & 0 & \kappa_n & 0 & 0 \\ 0 & 0 & -k_t d_0 & 0 & \kappa_t + k_t d_0^2 & 0 \\ 0 & k_t d_0 & 0 & 0 & 0 & \kappa_t + k_t d_0^2 \end{bmatrix},$$

$$\mathbf{K'}_{12} = \begin{bmatrix} -k_n & 0 & 0 & 0 & 0 & 0 \\ 0 & -k_t & 0 & 0 & 0 & k_t d_0 \\ 0 & 0 & -k_t & 0 & -k_t d_0 & 0 \\ 0 & 0 & 0 & -\kappa_n & 0 & 0 \\ 0 & 0 & k_t d_0 & 0 & k_t d_0^2 - \kappa_t & 0 \\ 0 & -k_t d_0 & 0 & 0 & 0 & k_t d_0^2 - \kappa_t \end{bmatrix},$$

$$\mathbf{K'}_{21} = \begin{bmatrix} -k_n & 0 & 0 & 0 & 0 & 0 \\ 0 & -k_t & 0 & 0 & 0 & -k_t d_0 \\ 0 & 0 & -k_t & 0 & k_t d_0 & 0 \\ 0 & 0 & 0 & -\kappa_n & 0 & 0 \\ 0 & 0 & -k_t d_0 & 0 & k_t d_0^2 - \kappa_t & 0 \\ 0 & k_t d_0 & 0 & 0 & 0 & k_t d_0^2 - \kappa_t \end{bmatrix},$$

$$\mathbf{K'}_{22} = \begin{bmatrix} k_n & 0 & 0 & 0 & 0 & 0 \\ 0 & k_t & 0 & 0 & 0 & -k_t d_0 \\ 0 & 0 & k_t & 0 & k_t d_0 & 0 \\ 0 & 0 & 0 & \kappa_n & 0 & 0 \\ 0 & 0 & k_t d_0 & 0 & k_t d_0^2 + \kappa_t & 0 \\ 0 & -k_t d_0 & 0 & 0 & 0 & k_t d_0^2 + \kappa_t \end{bmatrix}.$$

The first step to assemble the global stiffness matrix is to perform the coordinate transformation on $\mathbf{K'}_{11}$, $\mathbf{K'}_{12}$, $\mathbf{K'}_{21}$, $\mathbf{K'}_{22}$ of every constructed beam element. The coordinate transformation of each block of the stiffness matrix could be done only on their tensorial form; therefore, the 6×6 blocks of stiffness matrix must first convert to $3 \times 3 \times 3 \times 3$ fourth-order tensorial form ($\mathrm{K'}_{ijkl}$). Each one of these fourth-order tensors must undergo coordinate transformation using the following equation:

$$\mathrm{K'}_{ijkl} = R_{im} R_{jn} R_{kp} R_{lq} \mathrm{K'}_{mnpq}, \quad \mathbf{R} = \mathbf{R}_z(\psi)\mathbf{R}_y(\phi)\mathbf{R}_x(\theta), \tag{6}$$

where $\mathbf{R}_x$, $\mathbf{R}_y$, and $\mathbf{R}_z$ are rotation matrices. After coordinate transformation, the global stiffness matrix could be obtained by assembling every block of the local stiffness matrix into their corresponding position in $6\mathrm{N} \times 6\mathrm{N}$ global stiffness matrix (N is the number of sintered particles). After subjecting every direction of every particle to either displacement or tractional boundary condition (BC), we could solve for displacement by inverting the global stiffness matrix.

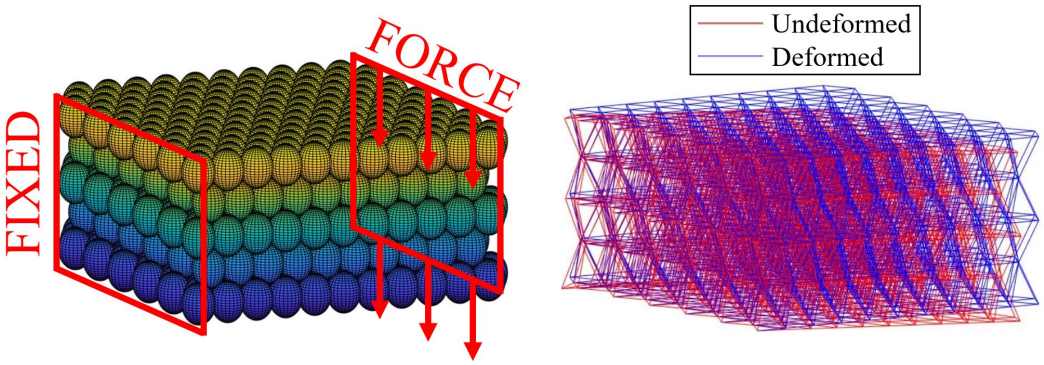

Figure 2 HCP structure for 0.25 mm × 0.25 mm × 0.1 mm AM part subjected to displacement and traction BC (left), deformed and undeformed generated spaceframe structure (right).

4 Simulation of Powder Bed Packing

In this section, we present a simple model of powder bed packing for elastic DEM analysis of powder-based AM structure. A number of researchers utilized Monte Carlo (MC) simulation to generate the random packing of unequal spherical particles [12]-[3]. The generated powder bed model by MC method was successfully used in the simulation of thermal behavior of AM processes (see [8]-[20]-[43]); Although these MC methods could not guarantee the structural determinacy of AM structure, they could generate a system of particles with complex stiffness values ($a^* > 1$). In this work, a simple Hexagonal Closest Packed (HCP) structure has been used to simulate the powder bed packing; consequently, the generated structure would be structurally determinant. To create a 3D HCP structure with unequal spherical particles, first, a completely packed 2D structure of uniform circular particle with radius lower than the desired average radius of particles generated then the second layer of powders could be generated by connecting the centers of the neighboring particles in the first layer and constructing 2D triangular elements. Consequently, the particles in the second layer can be generated at the center of each triangular element. The next layer of particles could be simply generated by copying the position of the particles from already generated first and second layers.

Each particle in the generated HCP structure just touching its neighboring particle, although these particles are not yet sintered together, and therefore the beam element could not be constructed between them. In order to create a realistic model of sintered particles, the radius of each particle in the HCP structure increased randomly between 5% to 14% of the radius of each particle. The increase in powder radii could not be set to more than 14% because it would cause the stiffnesses (Eq. (1) to Eq. (4)) to be complex numbers ($a^* > 1$). To ensure that this HCP model resembles the real sintered powder-based structure the position of each powder particle randomly changes within a small cubic box. The center of these cubic boxes is defined at the center of each undisplaced particles in the HCP structure, and each side of these boxes is $l = 2.05R_i$.

To model the geometry of the final product, a code was developed that first generates a fully packed HCP structure, then the powders that are not within the prescribed scanning path of the laser are deleted. Schematic of the laser scanning path on 3 mm × 3 mm domain. Figure 3 shows the scanning path on the AM structure, the red area is packed with particles, and there are no particles in the white space. The average radius of the spherical particle is set to be 12.5 μm.

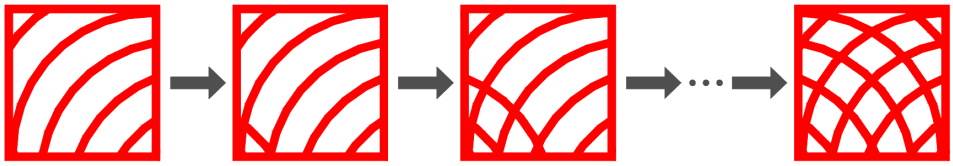

Figure 3 Schematic of the laser scanning path.

5 Microstructural Stress and Strain Tensor of Granular Assemblies

Because of the discrete nature of AM structure, the definition of continuum mechanical state variables stress and strain tensors are not self-evident. There are different approaches to find a theoretically correct definition of state variables based on grain displacements, local geometrical characteristics, and forces transmitted between contacting particles. In this work, we used the Katalin Bagi [2]-[1] definition of state variables in a granular assembly to obtain a volume average of stress and strain in the DEM simulation.

Bagi used the concept of *material cell* and *space cell* systems to discretize the unit normal vector in the Gauss-Ostrogradski equation and obtained the volume average of displacement gradient tensor as follows:

$$\bar{e}_{ij} = \frac{1}{V}\iiint\limits_{(V)} e_{ij}dV = \frac{1}{V}\iint\limits_{(S)} u_i n_j dS = \frac{1}{V}\sum_{m<n} \Delta u_i^{mn} d_j^{mn}, \tag{7}$$

where V is the volume of all constructed tetrahedral by beam elements and $\Delta u_i^{mn} = u_i^m - u_i^n$ is the relative displacement vector between every pair of particles obtained from already developed force-displacement DEM code, and d_j^{mn} is the *complimentary area vector* that can be defined as:

$$d_i^{mn} = \frac{1}{4}\sum_{t=1}^{T}\left(a_i^{m(t)} - a_i^{n(t)}\right), \quad a_i^k = -\frac{1}{3}b_i^k, \tag{8}$$

where particle (grain) G_m and G_n are sintered together, and the beam element is constructed between the centers of two particles. Now, all tetrahedral (space cells) that contain edge mn must be collected to calculate the complimentary area vector. In Eq. (1) T is the number of collected tetrahedral for edge mn and b_i^k is a vector corresponding with each four-face of every collected tetrahedron (the number of b_i^k vector for edge mn would be equal to $4T$). For instance, in Figure 4 three tetrahedral surrounding the edge $mn\,(T = 3)$. The magnitude of b_i^k vector is equal to the area of its corresponding face and the direction of this vector is normal to the face and pointing outward. The symmetric part of the displacement gradient would be the strain tensor.

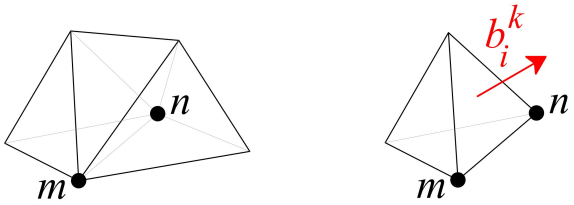

Figure 4 Schematic of three tetrahedral between six sintered particles (left), and the b_i^k (right).

Bagi expressed the Cauchy stress tensor for granular material with volume V as a summation of the dyadic product of contact forces between particles f_i^c and branch vector $(l_j^c = x_j^m x_j^n)$ as follows:

$$\bar{\sigma}_{ij} = \frac{1}{V} \iiint_{(V)} \sigma_{ij} dV = \frac{1}{V} \sum_{b \in B} f_i^b x_j^b = \frac{1}{V} \sum_{c \in V \cup B} f_i^c l_j^c, \tag{9}$$

where b is the number of particles subjected to external loading, and c is the number of contacts between powder particles. The effective elastic constants could be evaluated by performing six independent experiments for the same structure with different boundary conditions [22]. The effective compliance matrix $\mathbf{S}^{\text{eff}}$can be defined as follows:

$$\bar{\boldsymbol{\varepsilon}} = \mathbf{S}^{\text{eff}} \bar{\boldsymbol{\sigma}}. \tag{10}$$

The six general elastic properties (E_x, E_y, E_z, ν_{yz}, ν_{xz}, ν_{xy}) can be obtained from elements of the compliance matrix.

6 The Dataset and Pre-processing

The proposed method for the homogenization of elastic properties of powder-based AM structures in Sections 2 to 5 is not fast enough for developing a real-time control system capable of predicting the elastic properties of the aggregate at any given stage of manufacturing processes. In this section, an alternative approach to the homogenization of the powder-based AM structure presented using the CNN technique. The CNN that was initially introduced by Lecun et al. [16]-[18] has become an essential neural network architecture for computer vision tasks and image possessing. Local and global patterns of an image can be extracted with a convolutional layer; therefore, by nesting many convolutional layers in a hierarchical manner, CNN attempt to extract a broader structure from an image. The first step for implementing the CNN is to gather and prepare a dataset including hundreds of image representations of 3D printed structures and their corresponding elastic properties (E_x, E_y, E_z, ν_{yz}, ν_{xz}, ν_{xy}).

An image representation of powder-based AM structure could easily be obtained by discretizing the AM structure with small uniform cuboid boxes and calculating the fraction of the volume of each box filled with powders to the total volume of the box. For example, a structure with 3mm × 3mm base and three layers of powder could be discretized with 0.03mm × 0.03mm × 0.1mm cuboid; therefore, the structure would be turned into a 100×100 2D array of numbers (image) where each element of this array would be a number between 0 (empty cell) and 1 (fully-packed cell). Each one of these pixelated structures could be labeled with their corresponding elastic properties obtained with a time-consuming DEM homogenization process.

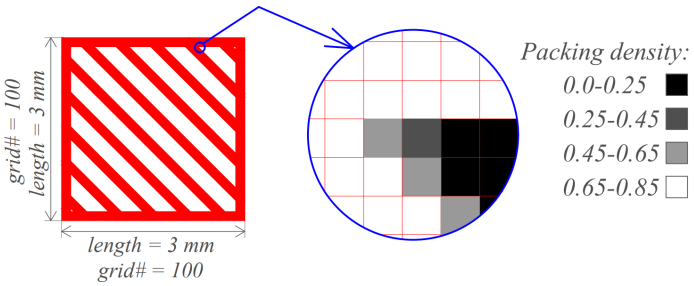

Figure 5 The pixelation process to present the AM structure with a 2D array of numbers.

7 Estimating the Effective Elastic Properties using CNN

CNN is an essential tool of deep learning, and it has demonstrated exceptional prediction performance within the field of computer vision [15]-[29]. CNN extracts features from images (2D or 3D arrays of numbers) and uses the backpropagation algorithm to optimize the learnable parameters in the network (weights and biases) [44]. Usually, CNN architecture contains multiple nested convolutional and pooling layers; subsequently, the data get flattened and passed into stack of fully connected layers [38].

The building blocks of convolutional layers are small learnable matrices called filters, which are used to extract the spatial features from the input array using the convolution operation. In order to create a complex decision boundary, the output of the convolutional operation would be passed into a nonlinear activation function. The typical activation function in a deep CNN architecture is the Rectified Linear Unit (ReLU) because of its short backpropagation's computational time compared to other nonlinear activation functions such as $tanh$ [19].

In order to reduce the number of extracted features and consequently decrease the number of learnable parameters, the output of the nonlinear activation function would be passed into a pooling layer. The most common form of pooling in CNN architectures is max pooling since it is extracting the most important features while reducing the size of the input. In order to extract meaningful data from pixel data, convolutional operation, activation function, and pooling operation must be stacked together [39].

Typically, the fully connected (FC) layers are the last part of CNN architectures [42]. All the neurons in the FC layers are connected to all the units of the previous layer. This full connection between input and output gives the model the ability to thoroughly mix the flow of information between the input and output of the FC layer; Therefore, the final output of CNN would be based on the whole image. The last FC layer (output layer) of conventional CNN architectures for multi-classification tasks would have a softmax activation function that computes the probability values of each class due to its mathematical definition. This means that by using the softmax activation function, the sum of the output values would be equal to 1 [14]. Although, in this work, we're trying to estimate the six independent, effective elastic properties of given pixelated AM structures; Hence, we modified the standard CNN architecture by replacing the classifier output layer with a multiple output linear regression layer. For a CNN with T outputs, where each output corespond to a distinct regression task, all T tasks share the same N input pixelated AM structures $\{x_i\}_{i=1}^{N}$, but have different class label $\{\{y_i^t\}_{i=1}^{N}\}_{t=1}^{T}$ [25]. Assuming every task (output) having same importance coefficient, the mean squared error loss function of the multiple output CNN regressor can be written as follows:

$$J(W,b) = \frac{1}{N}\sum_{i=1}^{N}\sum_{t=1}^{T}\left(y_i^t - \hat{y}_i^t\right)^2 \tag{11}$$

where $\hat{y}_i^t$ is the output of t-th regression task for i-th pixelated AM structures. Also, W and b are the weight and bias parameters of filters and FC layers for the entire CNN architecture that must be leaned using the backpropagation algorithm.

The output layer of several well-known deep CNN architectures for the multi-classification task (AlexNet [15], LeNet-5 [17], and VGG Net [32]) is replaced with the above proposed multiple output linear regression layer and used for training. These modified networks are backpropagated on proposed loss (error between predicted and actual effective elastic properties of AM structure) and optimized using an adaptive moment estimation (Adam)

algorithm. The original dataset is randomly split into 1600 training examples, and 400 of the original AM structures are used for validation purposes. All hyperparameters were kept as Keras API's default value except the batch size, which set to be 100 training examples for each iteration.

Training the modified AlexNet, LeNet-5, and VGG Net for 80 epochs results in training accuracy of 92.5%, 90.6%, and 18.1%, respectively. Despite the VGG Net's enormous number of trainable parameters (65.07 million parameters), its accuracy is very limited for our task. VGG Net's poor performance might be caused by vanishing gradient issues in very deep neural networks [34] or might be caused by the small number of training examples. The AlexNet with 20.31 million and LeNet-5 with only 59 thousand trainable parameters perform way better than the VGG Net. Although even with AlexNet's smaller number of parameters compared to VGG Net, the forward propagation process for an unseen AM structure might not be fast enough for a real-time control system. The LeNet-5 computational time for forward propagation is shorter than AlexNet, although it's less accurate. In order to achieve high accuracy and acceptable computational efficiency, we propose a new CNN architecture called Custom Net optimized for homogenization of aggregate elastic properties of powder-beds.

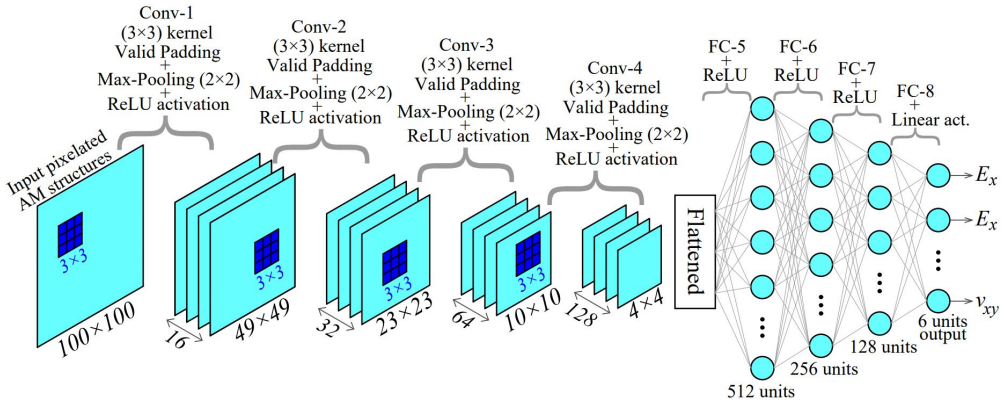

Figure 6 The CNN architecture of the proposed Custom Net.

As shown in Figure 6, the Custom Net consists of four stacks of convolutional operation, ReLU activation function, and pooling operation followed by four FC layers. The three hidden FC layer has ReLU activation function, and the last FC layer uses the multiple output linear regression layer. All convolutional (Conv) layer has the same 3×3 kernels, and the number of Channels gradually increases from 16 in Conv-1 to 128 in Conv-4. Every Max-Pooling operation has a 2×2 filter, and the number of units in FC layers reduces from 512 units in FC-5 to 128 units in FC-7. The Custom Net trained with the same optimizer and hyperparameters used for training of the three well-known deep CNN architectures.

The 1.31 million trainable parameters of the proposed Custom Net is significantly smaller than VGG Net and AlexNet's parameters. Therefore, Custom Net is easier to train and faster to implement for an unseen example compared to other architectures. Figure 7 illustrates the loss versus the number of batches of data that feed into all four CNN architectures, and one can see that the Custom Net converged faster than the other three CNN architecture, and after 1200 batch of training example Custom Net is more accurate than Alex Net and LeNet-5. The Training and validation accuracy of Custom Net over the increasing number of epochs (training iterations) are shown in Figure 8. After training the Custom Net for

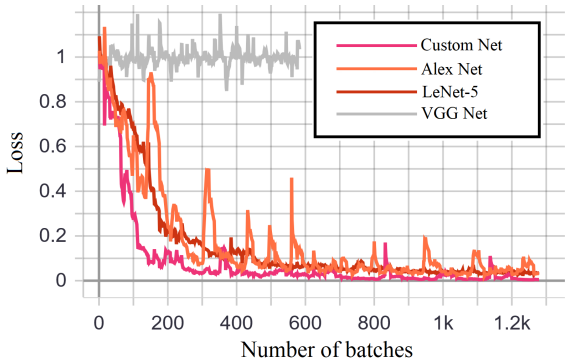

Figure 7 Loss (error) Vs. the number of batches of data for AlexNet, LeNet-5, VGG Net, and proposed Custom Net.

80 epochs, it's performing 96.5% accuracy on the training set and 96.1% accuracy on the validation set. The negligible difference between training and validation accuracy shows that this model has a low variance; therefore, the additional overfitting prevention strategies (dropout, regularization, and data augmentation) are unnecessary.

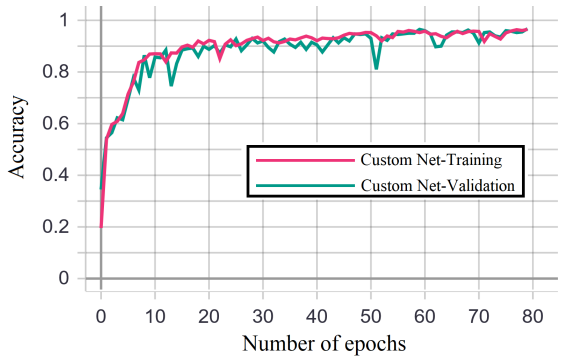

Figure 8 Training and validation accuracy versus the number of epochs for Custom Net.

For this specific dataset, the Custom Net takes 32 minutes to get trained, and on average, it takes 37.24 millisecond for Custom Net to predict the effective elastic properties of an unseen powder-bed structure. The computational time for the prediction of effective elastic properties of Custom Net is significantly shorter compared to the original DEM code (51 minutes for structure with the small number of particles and 6 hours and 34 minutes for a large number of particles).

8 Numerical examples

Several examples are presented here to verify the accuracy of the proposed CNN model for the estimation of the aggregate elastic properties of powder-beds. The described DEM model in Sections 2 to 5 is used to generate the dataset and Custom Net CNN architecture used for subsecond prediction of effective properties of the same structures. The material properties of the powder particle used to generate the dataset are listed in Table 1.

Figure 9 and Figure 10 compare the effective elastic properties evaluated by the DEM method with their corresponding predicted values using the proposed CNN method for 400 different powder-bed structures in the validation set. In general, the effective modulus

Table 1 Material properties of powder particles [9].

Property	Value
Particle mean radius (R_i)	12.5 μm
Density (ρ_i)	7800 Kg/m^3
Young's modulus (E_i)	210 GPa
Poisson's Ratio (ν_i)	0.28

of elasticity (E_x, E_y, E_z) gets larger as the packing density of the powder-bed structures increases; although, the expansion of the packing density would not necessarily cause an increase in Poisson's ratio (ν_{yz}, ν_{xz}, ν_{xy}). It is worth noting that the cubic fit to DEM evaluated, and CNN predicted values shown in Figure 9, and Figure 10 are not reflecting any fixed set of mathematical relationships. Therefore, the fast estimation of the effective elastic property of an unseen powder-bed structure could only be done with the help of forward propagation through the already trained CNN model.

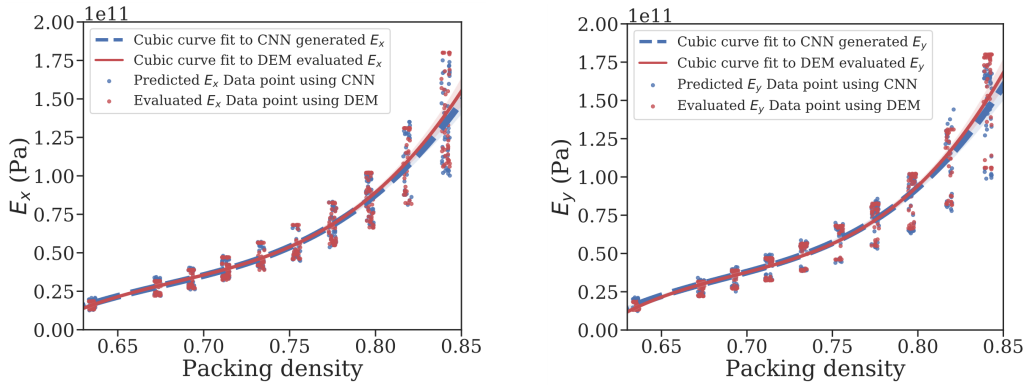

Figure 9 Scatterplot of DEM evaluated, and CNN predicted E_x (left) and E_y (right) versus Packing density validation set. The cubic fit to DEM evaluated, and CNN predicted values is also included.

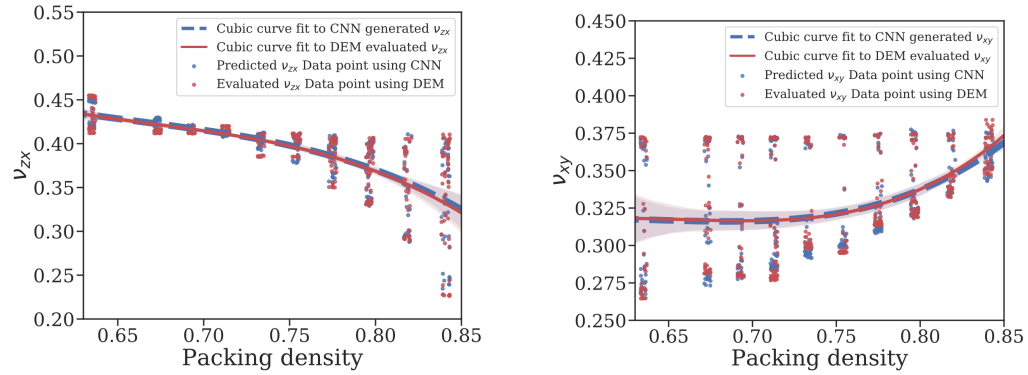

Figure 10 Scatterplot of DEM evaluated, and CNN predicted ν_{zx} (left) and ν_{xy} (right) versus Packing density validation set. The cubic fit to DEM evaluated, and CNN predicted values is also included.

Based on the results shown in Figure 9 and Figure 10, the CNN model has higher accuracy for powder-bed packing structures with lower packing density.

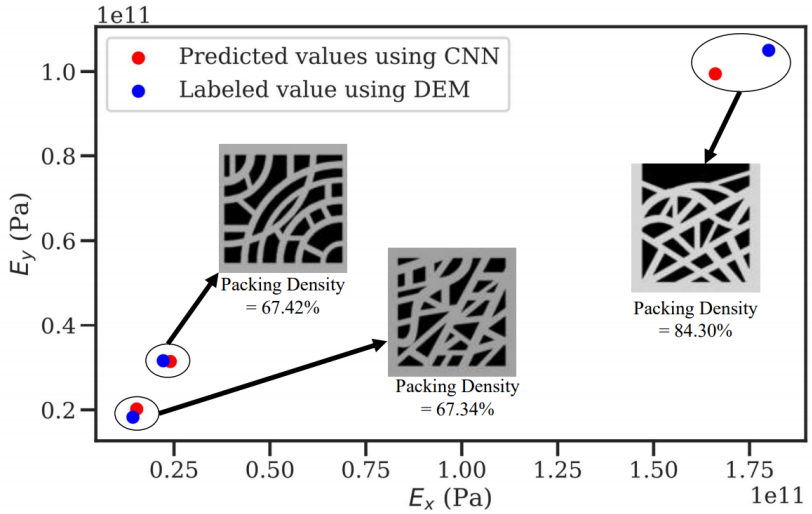

Figure 11 Scatterplot of DEM evaluated, and CNN predicted E_x versus E_y for three different powder-bed structure.

Figure 11 and Figure 12 show a comprehensive comparison between DEM evaluated and CNN predicted values of modulus of elasticity and Poisson's ratio, respectively. In each of these two figures, three powder-bed packing structure randomly selected form validation set and a scatter diagram has been used to compare two different elastic properties (E_x, E_y in Figure 11 and ν_{xz}, ν_{yz} in Figure 12). Again one can see that the CNN model is more accurate for a powder-bed packing structure that has a smaller packing density.

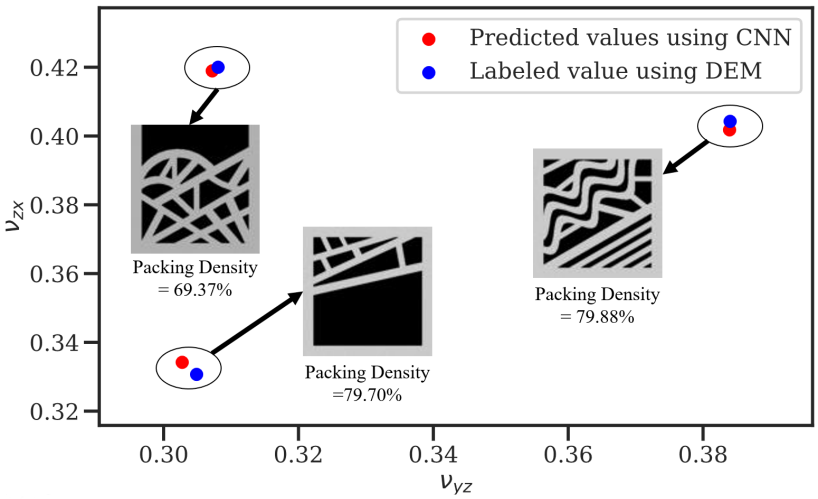

Figure 12 Scatterplot of DEM evaluated, and CNN predicted ν_{zx} versus ν_{yz} for three different powder-bed structure.

9 Conclusion and Future Work

In this work, a deep learning approach in the determination of aggregate elastic properties of powder-beds in AM structures is presented. The proposed approach has been verified by comparison with the results of DEM simulation, and for unseen powder-bed structures, the average difference in predicted elastic properties between the proposed CNN model and DEM simulation is less than 4%. The developed CNN model is much more efficient than DEM simulations because of the ability to predict the effective elastic properties without the construction of the large stiffness matrix. The computational time of CNN model is 0.0005% the time needed for solving the problem using DEM simulation. The developed CNN model will be very useful in the development of a real-time control system for predicting the aggregate elastic properties of powder-beds during the manufacturing process. The proposed CNN model is trained only for powder particles with properties listed in Table 1. In principle, a similar CNN model could be used for powder particles with different material properties by concatenating the material properties to flattened layers of CNN architecture as new neurons. Subsequently, the slightly modified CNN model must be trained using examples of powder-beds with different properties of powder particles.

References

1 K. Bagi. Microstructural Stress Tensor of Granular Assemblies With Volume Forces. *Journal of Applied Mechanics*, 66(4):934–936, December 1999. doi:10.1115/1.2791800.

2 Katalin Bagi. Stress and strain in granular assemblies. *Mechanics of Materials*, 22(3):165–177, March 1996. doi:10.1016/0167-6636(95)00044-5.

3 H. J. H. Brouwers. Particle-size distribution and packing fraction of geometric random packings. *Physical Review E*, 74(3):031309, September 2006. doi:10.1103/PhysRevE.74.031309.

4 F. Calignano, D. Manfredi, E. P. Ambrosio, L. Iuliano, and P. Fino. Influence of process parameters on surface roughness of aluminum parts produced by DMLS. *The International Journal of Advanced Manufacturing Technology*, 67(9):2743–2751, 2013. doi:10.1007/s00170-012-4688-9.

5 G. Casalino, S. L. Campanelli, N. Contuzzi, and A. D. Ludovico. Experimental investigation and statistical optimisation of the selective laser melting process of a maraging steel. *Optics & Laser Technology*, 65:151–158, January 2015. doi:10.1016/j.optlastec.2014.07.021.

6 Wei Gao, Yuanqiang Tan, and Mengyan Zang. A cubic arranged spherical discrete element model. *International Journal of Computational Methods*, 11(05):1350102, 2014. doi:10.1142/S0219876213501028.

7 Arash Gobal. *An Adaptive Discrete Element Method for Physical Modeling of the Selective Laser Sintering Process*. PhD thesis, UC Davis, 2017.

8 Arash Gobal and Bahram Ravani. An Adaptive Discrete Element Method for Physical Modeling of the Selective Laser Sintering Process, 2017. doi:10.4028/www.scientific.net/AMM.869.69.

9 Arash Gobal and Bahram Ravani. Physical Modeling for Selective Laser Sintering Process. *Journal of Computing and Information Science in Engineering*, 17(2), June 2017. doi:10.1115/1.4034473.

10 Dongdong Gu and Beibei He. Finite element simulation and experimental investigation of residual stresses in selective laser melted Ti–Ni shape memory alloy. *Computational Materials Science*, 117:221–232, 2016. doi:10.1016/j.commatsci.2016.01.044.

11 S. Haeri, Y. Wang, O. Ghita, and J. Sun. Discrete element simulation and experimental study of powder spreading process in additive manufacturing. *Powder Technology*, 306:45–54, January 2017. doi:10.1016/j.powtec.2016.11.002.

12 D. He, N. N. Ekere, and L. Cai. Computer simulation of random packing of unequal particles. *Physical Review E*, 60(6):7098–7104, December 1999. doi:10.1103/PhysRevE.60.7098.

13 George Jefferson, George K. Haritos, and Robert M. McMeeking. The elastic response of a cohesive aggregate—a discrete element model with coupled particle interaction. *Journal of the Mechanics and Physics of Solids*, 50(12):2539–2575, December 2002. doi:10.1016/S0022-5096(02)00051-0.

14 I. Kouretas and V. Paliouras. Simplified Hardware Implementation of the Softmax Activation Function. In *2019 8th International Conference on Modern Circuits and Systems Technologies (MOCAST)*, pages 1–4, May 2019. doi:10.1109/MOCAST.2019.8741677.

15 Alex Krizhevsky, Ilya Sutskever, and Geoffrey E Hinton. ImageNet Classification with Deep Convolutional Neural Networks. In F. Pereira, C. J. C. Burges, L. Bottou, and K. Q. Weinberger, editors, *Advances in Neural Information Processing Systems 25*, pages 1097–1105. Curran Associates, Inc., 2012. URL: http://papers.nips.cc/paper/4824-imagenet-classification-with-deep-convolutional-neural-networks.pdf.

16 Y. LeCun, B. Boser, J. S. Denker, D. Henderson, R. E. Howard, W. Hubbard, and L. D. Jackel. Backpropagation Applied to Handwritten Zip Code Recognition. *Neural Computation*, 1(4):541–551, December 1989. doi:10.1162/neco.1989.1.4.541.

17 Y. Lecun, L. Bottou, Y. Bengio, and P. Haffner. Gradient-based learning applied to document recognition. *Proceedings of the IEEE*, 86(11):2278–2324, 1998. Conference Name: Proceedings of the IEEE. doi:10.1109/5.726791.

18 Yann LeCun, Patrick Haffner, Léon Bottou, and Yoshua Bengio. Object Recognition with Gradient-Based Learning. In David A. Forsyth, Joseph L. Mundy, Vito di Gesú, and Roberto Cipolla, editors, *Shape, Contour and Grouping in Computer Vision*, Lecture Notes in Computer Science, pages 319–345. Springer, Berlin, Heidelberg, 1999. doi:10.1007/3-540-46805-6_19.

19 Hyungtae Lee and Heesung Kwon. Going Deeper With Contextual CNN for Hyperspectral Image Classification. *IEEE Transactions on Image Processing*, 26(10):4843–4855, October 2017. Conference Name: IEEE Transactions on Image Processing. doi:10.1109/TIP.2017.2725580.

20 Yousub Lee. *Simulation of Laser Additive Manufacturing and its Applications*. PhD thesis, The Ohio State University, 2015. URL: https://etd.ohiolink.edu/pg_10?0::NO:10:P10_ACCESSION_NUM:osu1440360229.

21 Xiaoxing Liu, Christophe L. Martin, Gérard Delette, and Didier Bouvard. Elasticity and strength of partially sintered ceramics. *Journal of the Mechanics and Physics of Solids*, 58(6):829–842, June 2010. doi:10.1016/j.jmps.2010.04.007.

22 Xingchen Liu and Vadim Shapiro. Homogenization of material properties in additively manufactured structures. *Computer-Aided Design*, 78:71–82, September 2016. doi:10.1016/j.cad.2016.05.017.

23 G. Miranda, S. Faria, F. Bartolomeu, E. Pinto, S. Madeira, A. Mateus, P. Carreira, N. Alves, F. S. Silva, and O. Carvalho. Predictive models for physical and mechanical properties of 316L stainless steel produced by selective laser melting. *Materials Science and Engineering: A*, 657:43–56, March 2016. doi:10.1016/j.msea.2016.01.028.

24 Mojtaba Mozaffar, Arindam Paul, Reda Al-Bahrani, Sarah Wolff, Alok Choudhary, Ankit Agrawal, Kornel Ehmann, and Jian Cao. Data-driven prediction of the high-dimensional thermal history in directed energy deposition processes via recurrent neural networks. *Manufacturing Letters*, 18:35–39, 2018. doi:10.1016/j.mfglet.2018.10.002.

25 Zhenxing Niu, Mo Zhou, Le Wang, Xinbo Gao, and Gang Hua. Ordinal Regression With Multiple Output CNN for Age Estimation. In *Proceedings of the IEEE Conference on Computer Vision and Pattern Recognition (CVPR)*, pages 4920–4928, 2016. URL: http://openaccess.thecvf.com/content_cvpr_2016/html/Niu_Ordinal_Regression_With_CVPR_2016_paper.html.

26 Eric J. R. Parteli and Thorsten Pöschel. Particle-based simulation of powder application in additive manufacturing. *Powder Technology*, 288:96–102, January 2016. doi:10.1016/j.powtec.2015.10.035.

27 Arindam Paul, Mojtaba Mozaffar, Zijiang Yang, Wei-keng Liao, Alok Choudhary, Jian Cao, and Ankit Agrawal. A real-time iterative machine learning approach for temperature profile prediction in additive manufacturing processes. *arXiv:1907.12953 [cs, stat]*, August 2019. arXiv: 1907.12953. URL: http://arxiv.org/abs/1907.12953.

28 Xinbo Qi, Guofeng Chen, Yong Li, Xuan Cheng, and Changpeng Li. Applying Neural-Network-Based Machine Learning to Additive Manufacturing: Current Applications, Challenges, and Future Perspectives. *Engineering*, 5(4):721–729, August 2019. doi:10.1016/j.eng.2019.04.012.

29 Mohammad Rastegari, Vicente Ordonez, Joseph Redmon, and Ali Farhadi. XNOR-Net: ImageNet Classification Using Binary Convolutional Neural Networks. In Bastian Leibe, Jiri Matas, Nicu Sebe, and Max Welling, editors, *Computer Vision – ECCV 2016*, Lecture Notes in Computer Science, pages 525–542, Cham, 2016. Springer International Publishing. doi:10.1007/978-3-319-46493-0_32.

30 Noriko Read, Wei Wang, Khamis Essa, and Moataz M. Attallah. Selective laser melting of AlSi10Mg alloy: Process optimisation and mechanical properties development. *Materials & Design (1980-2015)*, 65:417–424, January 2015. doi:10.1016/j.matdes.2014.09.044.

31 Luke Scime and Jack Beuth. A multi-scale convolutional neural network for autonomous anomaly detection and classification in a laser powder bed fusion additive manufacturing process. *Additive Manufacturing*, 24:273–286, December 2018. doi:10.1016/j.addma.2018.09.034.

32 Karen Simonyan and Andrew Zisserman. Very Deep Convolutional Networks for Large-Scale Image Recognition. *arXiv:1409.1556 [cs]*, 2015. arXiv: 1409.1556. URL: http://arxiv.org/abs/1409.1556.

33 A.K. Singh and Prakash Regalla Srinivasa. Response surface-based simulation modeling for selective laser sintering process. *Rapid Prototyping Journal*, 16(6):441–449, 2010. doi:10.1108/13552541011083362.

34 Rajwinder Singh, Rahul Rana, and Sunil Kr Singh. Performance Evaluation of VGG models in Detection of Wheat Rust, 2018. Library Catalog: www.semanticscholar.org. URL: /paper/Performance-Evaluation-of-VGG-models-in-Detection-Singh-Rana/01c8aa86f8d424f52b92efd1870caa5061bf7d64.

35 Bo Song, Shujuan Dong, Baicheng Zhang, Hanlin Liao, and Christian Coddet. Effects of processing parameters on microstructure and mechanical property of selective laser melted Ti6Al4V. *Materials & Design*, 35:120–125, March 2012. doi:10.1016/j.matdes.2011.09.051.

36 Ivar Stakgold and Michael J. Holst. *Green's Functions and Boundary Value Problems*. John Wiley & Sons, March 2011. Google-Books-ID: 8OeoISCW6qUC.

37 John C. Steuben, Athanasios P. Iliopoulos, and John G. Michopoulos. On Multiphysics Discrete Element Modeling of Powder-Based Additive Manufacturing Processes. In *Proceedings of the ASME 2016 International Design Engineering Technical Conferences and Computers and Information in Engineering Conference. Volume 1A: 36th Computers and Information in Engineering Conference*. American Society of Mechanical Engineers Digital Collection, 2016. doi:10.1115/DETC2016-59634.

38 Tian Wang, Yang Chen, Meina Qiao, and Hichem Snoussi. A fast and robust convolutional neural network-based defect detection model in product quality control. *The International Journal of Advanced Manufacturing Technology*, 94(9-12):3465–3471, February 2018. doi:10.1007/s00170-017-0882-0.

39 Daniel Weimer, Bernd Scholz-Reiter, and Moshe Shpitalni. Design of deep convolutional neural network architectures for automated feature extraction in industrial inspection. *CIRP Annals*, 65(1):417–420, January 2016. doi:10.1016/j.cirp.2016.04.072.

40 Yangzhan Yang, Madie Allen, Tyler London, and Victor Oancea. Residual Strain Predictions for a Powder Bed Fusion Inconel 625 Single Cantilever Part. *Integrating Materials and Manufacturing Innovation*, 8(3):294–304, 2019. doi:10.1007/s40192-019-00144-5.

41 Bodi Yuan, Brian Giera, Gabe Guss, Ibo Matthews, and Sara Mcmains. Semi-Supervised Convolutional Neural Networks for In-Situ Video Monitoring of Selective Laser Melting. In *2019 IEEE Winter Conference on Applications of Computer Vision (WACV)*, pages 744–753, January 2019. ISSN: 1550-5790. doi:10.1109/WACV.2019.00084.

42 Chen-Lin Zhang, Jian-Hao Luo, Xiu-Shen Wei, and Jianxin Wu. In Defense of Fully Connected Layers in Visual Representation Transfer. In Bing Zeng, Qingming Huang, Abdulmotaleb El Saddik, Hongliang Li, Shuqiang Jiang, and Xiaopeng Fan, editors, *Advances in Multimedia Information Processing – PCM 2017*, Lecture Notes in Computer Science, pages 807–817, Cham, 2018. Springer International Publishing. doi:10.1007/978-3-319-77383-4_79.

43 Z. Zhang, Z. J. Tan, X. X. Yao, C. P. Hu, P. Ge, Z. Y. Wan, J. Y. Li, and Q. Wu. Numerical methods for microstructural evolutions in laser additive manufacturing. *Computers & Mathematics with Applications*, 78(7):2296–2307, October 2019. doi:10.1016/j.camwa.2018.07.011.

44 Anwen Zhu, Xiaohui Li, Zhiyong Mo, and Ruaren Wu. Wind power prediction based on a convolutional neural network. In *2017 International Conference on Circuits, Devices and Systems (ICCDS)*, pages 131–135, September 2017. doi:10.1109/ICCDS.2017.8120465.